Main Manuscript for

Electrical control of the transduction channels' gating force in sensory hair cells.

Achille Joliot[a,b], Laure Stickel[a,b] and Pascal Martin[a,b,*]

[a] Physique des Cellules et Cancer, Institut Curie, PSL Research University, CNRS UMR168, F-75248 Paris, France.

[b] Sorbonne Université, F-75252 Paris, France.

[*] Correspondence: pascal.martin@curie.fr

Competing Interest Statement: The authors declare no conflict of interest.

Keywords: auditory system, bioelectricity, gating compliance, mechanosensitive ion channels, vestibular system.

This PDF file includes:

Main Text

Figures 1 to 5

ABSTRACT

Hair cells, the sensory receptors of the inner ear, rely on mechanosensitive ion channels to transduce mechanical vibrations of their hair bundle into electrical signals. The mechanical correlate of channel gating—the gating force—is a fundamental determinant of hair-cell mechanosensitivity to displacements of the hair bundle. We report here the effects of varying the electrical potential across the epithelium that houses the hair cells on the gating force. We found that a negative potential in the endolymph that bathed the hair bundles increased the gating force by up to twofold, while positive endolymphatic potentials had the opposite effect. In contrast, the endolymphatic potential only weakly affected hair-bundle stiffness. Together, our results indicate that the gating force varied because the gating swing varied, from values that are comparable to the pore size of the transduction channels to values nearly tenfold as large. When the endolymphatic potential reached a negative threshold value of about -50 mV, our work further revealed a reversible, but hysteretic, transition between states of strong and weak gating force, for which the hair bundles oscillated spontaneously or remained quiescent, respectively. Finally, we provide evidence that these effects resulted from a modulation of the Ca^{2+} influx through the transduction channels and that a minimal influx is necessary to produce strong gating forces. We propose that force sensitivity of the transduction channel protein complex can be adjusted by the hair cell depending on physiological control parameters.

SIGNIFICANCE STATEMENT

The inner ear's hair cells rely on mechanosensitive ion channels to convert vibrations of their hair bundles into electrical signals. We show that varying the electrical potential across the sensory hair-cell epithelium continuously modulates a fundamental determinant of mechanosensitivity called the gating force. Remarkably, a hair cell can also switch between states of weak and strong gating force at negative potentials, so that strong gating forces associated to high mechanosensitivity are observed only when the calcium influx through the channels is large enough, but not too large. Gating-force control is expected to underly the ear's ability to achieve exquisite mechanosensitivity to minute sound stimuli and be relevant to biological systems relying on direct mechanical gating of ion channels.

53 **INTRODUCTION**

54 In the inner ear, mechanoreception by the sensory hair cells starts with the deflection of their
55 hair bundle—a cohesive tuft of cylindrical protrusions called stereocilia that are arranged in a
56 staircase pattern (1–3). A deflection towards the taller row of stereocilia increases mechanical
57 tension in the oblique tip links that interconnect the tip of each stereocilium to the flank of a
58 taller neighbor, opening mechanosensitive ion channels, and evoking an influx of cations into
59 the hair cell, mostly of K^+ ions but also of Ca^{2+} ions.

60 Our understanding of hair-cell mechanosensitivity is informed by the gating-spring model
61 of mechanoelectrical transduction (4, 5). Within this framework, the transduction channels are
62 gated directly by force, which is transmitted to the channels via elastic elements—the gating
63 springs—that operate in series with the tip links. The product of the gating-spring stiffness and
64 the gating swing defines the gating force, a fundamental determinant of hair-cell
65 mechanosensitivity: its magnitude sets the maximal slope of the sigmoidal relation between the
66 transduction current and the deflection of the hair bundle (SI Appendix Fig. S1A-B). The
67 greater the gating force, the larger the transduction current evoked by a small stimulus, making
68 the hair cell more sensitive to a given deflection of its hair bundle.

69 The gating-spring model imposes a reciprocal relationship between tip-link tension and
70 channel gating. If tensioning the tip links evokes channel opening, then channel opening must
71 reduce tip-link tension by an amount given precisely by the mechanical correlate of channel
72 gating—the gating force. Feedback between tip-link tension and channel gating produces gating
73 compliance, the effective softening of the hair bundle upon channel gating (6, 7). For large
74 positive or negative bundle displacements, at which the transduction channels are respectively
75 nearly all open or closed, the force-displacement relation is linear. At intermediate
76 displacements that elicit gating of the transduction channels, however, the slope of the force-
77 displacement relation is reduced: the hair bundle is effectively softer. Gating compliance is
78 associated with a shift between the two linear limbs of the force-displacement relation; this shift
79 provides an estimate of the combined gating force, denoted F_G in the following, produced by
80 the ensemble of transduction channels that operate in parallel within the hair bundle (SI
81 Appendix Fig. S1B). Furthermore, upon an oscillatory movement of the hair bundle, opening
82 and closing of the transduction channels also increase friction on the hair bundle, a phenomenon
83 called gating friction (8). The experimental demonstration of gating compliance and gating
84 friction provides strong support for the gating-spring model.

With hair cells in excised preparations of the mammalian cochlea, gating forces can be so weak that the force-displacement relation remains linear (9, 10), although there is also evidence that hair-bundle mechanics can be nonlinear (11–13). In the frog saccule, depending on ex-vivo conditions, gating forces can lead to a moderate (about 40%) decrease in hair-bundle stiffness (6) or, remarkably, be strong enough to result in negative stiffness, which can lead to spontaneous oscillations of the hair bundle and frequency-selective amplification of periodic stimuli (14–17). The magnitude of the gating force thus appears to be variable. The mechanism that sets and controls the gating force has remained elusive, despite its importance for mechanosensitivity of the hair cell.

In this work, we estimate the gating force, as well as the size of the molecular movement associated to channel gating—the gating swing, from nonlinear-stiffness and friction measurements at the micron-sized scale of a hair bundle. We report that the electrical potential across the sensory epithelium that houses the hair cells can serve as a control parameter of the gating force. Our work further reveals a reversible, but hysteretic, transition between a state of strong gating force, for which the hair bundles oscillate spontaneously, and a state of weak gating force, for which hair-bundle mechanics is linear and the hair bundles are quiescent. We finally provide evidence that these effects are mediated by the influx of Ca^{2+} through the transduction channels.

RESULTS

We took advantage of an excised preparation of the frog saccule that mimics *ex vivo* the two-compartment ionic conditions that the sensory epithelium experiences *in vivo*. Under these conditions, the hair cells routinely displayed spontaneous oscillations of their hair bundles, as recognized before (18–20). We aimed here at evaluating the effects of a transepithelial potential on hair-bundle mechanics. To this end, we used a pair of electrodes and a current generator to impose a transepithelial current, I, within a range of ± 10 μA (SI Appendix Fig. S2A). Upon application of a current step, the transepithelial potential, U, reached a steady-state value in about 600 μs (SI Appendix Fig. S2B). As a rule of thumb, a positive current of $+1$ μA evoked a positive potential in the endolymphatic compartment of $+10$ mV with respect to the perilymphatic compartment; accordingly, the transepithelial potential thus varied within a range of ± 100 mV. We emphasize for the following that a positive endolymphatic potential is expected to increase the influx of K^+ and Ca^{2+} ions through the transduction channels, whereas

116 a negative potential does the opposite. All numerical results are given below as the average and
117 standard deviations (SD) over an ensemble of n independent measurements.

118 **Strong modulation of the gating force, weak modulation of the hair-bundle stiffness.**

119 To determine the effects of an endolymphatic potential on the mechanical properties of a hair
120 bundle, we measured the bundle's force-displacement relation in response to a series of step
121 displacements applied to the base of a stimulus fiber (Fig. 1). Under control conditions, for
122 which no transepithelial current was applied ($I = 0$), a fit of the relation to Equation 1
123 (Methods) yielded a set-point deflection $X_0 = -2 \pm 7$ nm, a gating force $F_G = 17 \pm 4$ pN and
124 a linear stiffness $K = 0.85 \pm 0.2\ \mathrm{pN} \cdot \mathrm{nm}^{-1}$ (mean ± SD; $n = 29$ in 16 frogs). We recall that
125 the set-point deflection is interpreted as the deflection that leads to a channels' open probability
126 of ½ (15). For each hair bundle, the procedure was repeated in the presence of a static
127 transepithelial current ($I \neq 0$).

128 We start by presenting the effects of a transepithelial current on a force-displacement relation
129 in four representative examples (Fig. 1); the effects on the corresponding spontaneous hair-
130 bundle oscillations are shown in SI Appendix (Fig. S3A-D). Applying a positive current, here
131 $I = +3$ μA, corresponding to a positive endolymphatic potential, $U \simeq +30$ mV, evoked an
132 increase of the set-point deflection: the transduction channels closed (Fig. 1A). In addition, we
133 observed a small (-5%) decrease of the linear bundle's stiffness and, remarkably, a large
134 decrease (-38%) of the gating force. In another cell, a larger current $I = +6$ μA resulted in a
135 similar change in stiffness (-6%) but evoked a larger decrease of the gating force (-50%;
136 Fig. 1B). Conversely, applying a negative current of moderate magnitude, here $I = -3$ μA,
137 corresponding to a negative endolymphatic potential, $\mathrm{U} \simeq -30$ mV, elicited a decrease of the
138 set-point deflection and thus opening of the transduction channels, a small increase ($+10\%$) of
139 the linear stiffness, and a large increase ($+89\%$) of the gating force (Fig. 1C). Furthermore,
140 applying a large transepithelial current, here $\mathrm{I} = -6$ μA, led to an unexpected finding: the force-
141 displacement relation became linear (Fig. 1D). This is not because the integrity of the hair cell
142 was impaired by application of a large transepithelial current, for all the effects were fully
143 reversible.

144 Performing an ensemble of $n = 41$ pairs of measurements in 29 hair bundles from 16 frogs
145 confirmed the effects illustrated by the four representative examples. We found a strong positive
146 correlation between the change, $\Delta X_0 = X_0(I) - X_0(I = 0)$, of the set-point deflection and the
147 applied transepithelial current (Fig. 2A). This correlation came as no surprise for the

endolymphatic potential resulting from the transepithelial current should influence the magnitude of the Ca^{2+} influx through the transduction channels and calcium is known to promote channel closure (4, 15, 21–23). The change in linear stiffness, $\Delta K = K(I) - K(I = 0)$, was negatively correlated to the transepithelial current, but only weakly (Fig. 2B). Instead, for currents $I > -4$ μA, the change, $\Delta F_G = F_G(I) - F_G(I = 0)$, of the hair-bundle's gating force displayed a strong negative correlation with the current (Fig. 2C). The relative variation of the gating force was correspondingly much larger than that of the linear stiffness (Fig. 2D). A positive transepithelial current evoked a reduction of the gating force by as much as -80%, whereas the stiffness decreased at most by -10% over the same range of transepithelial currents. Conversely, the gating force could nearly double in the presence of a negative transepithelial current, corresponding to a relative increase of $+100\%$, whereas stiffness did not increase beyond $+25\%$. These correlations between mechanical properties of the hair bundle and the transepithelial current were associated to systematic changes of the frequency, amplitude and waveform of spontaneous hair-bundle oscillations (SI Appendix Fig. S3E-G).

For all the seven hair bundles for which the transepithelial current was more negative than -5 μA, corresponding to an endolymphatic potential $U \leq -50$ mV, the gating force did not follow the trend observed at more positive potentials. Instead of increasing further or saturating at more negative potentials, the gating force dropped to values so low that the force-displacement relation was linear, thus with no detectable signature of gating compliance (Fig. 1D and Fig. 2C and D). At these endolymphatic potentials, no spontaneous oscillation was observed; the hair bundles were quiescent (SI Appendix Fig. S3D). Our study thus revealed the existence of a critical value of the endolymphatic potential, $U = U_C \simeq -50$ mV, that delimited two states of the hair bundle: a state of strong gating force for which gating compliance was large enough to yield spontaneous oscillations of the hair bundle and a state of weak gating force for which hair-bundle mechanics was linear and the hair bundle was quiescent.

Hysteretic transition between states of strong and weak gating force.

To further explore the transition between states of strong and weak gating force (Fig. 1D and Fig. 2C), we applied ramps of transepithelial current (Fig. 3A) while the hair bundle was subjected to triangular mechanical stimulation (Fig. 3B). This stimulation protocol allowed to monitor, continuously for the same hair bundle, how the mechanical properties varied as a function of the transepithelial current. The ramps were slow enough that the transepithelial current varied by only ~0.2 μA over the time required to measure a force-displacement cycle

180 (see Methods). Because this variation was too small to elicit a significant variation of the gating
181 force (Fig. 2D), the mechanical measurements were quasi static. The mechanical stimulus
182 elicited a force-displacement cycle with clockwise circulation, corresponding to energy
183 dissipation (8). The cycle displayed a region of lower slope—gating compliance—on the
184 positive and negative half cycles (Fig. 3C), where the channels opened and closed, respectively.
185 In addition, the height of the force-displacement cycle was larger within the region of channel
186 gating. This property was previously shown to result from the contribution of the transduction
187 channels' gating force to hair-bundle friction, a phenomenon called gating friction, and the
188 displacement at which the cycle had a maximal height (abscissa of disks in Fig. 3C) was
189 identified as the set-point deflection, X_0 (8). In the following, the maximal half-height of the
190 cycle, ϕ_{MAX}, was used as a reporter for the magnitude of the gating force.

191 As the transepithelial current decreased from zero to negative values, the region of gating
192 compliance and gating friction in the force-displacement cycle shifted toward more negative
193 displacements, corresponding to a decrease of the set-point deflection and thus opening of the
194 transduction channels (Fig. 3C, SI Appendix Movie S1). Following the point of inversion
195 symmetry in a force-displacement cycle resulted in a nearly linear trajectory of slope $0.4 \pm$
196 $0.2\ \mathrm{pN} \cdot \mathrm{nm}^{-1}$ ($n = 8$; Fig. 3D). In addition, the height of the force-displacement cycle, and
197 thus the maximal friction force, ϕ_{MAX}, increased before saturating (Fig. 3E). When the absolute
198 magnitude of the negative current became large enough, corresponding to $I \leq I_C = -3.7 \pm$
199 $1\ \mu\mathrm{A}$ and an endolymphatic potential $U \leq U_C \simeq -37 \pm 10\ \mathrm{mV}$ ($n = 8$), the friction force ϕ_{MAX}
200 dropped (Fig. 3E-F, SI Appendix Movie S1) until the nonlinearity vanished (Fig. 3C, red).
201 These observations on single hair cells (solid line in Fig. 3E) mirrored the measured changes of
202 the gating force upon application of a static transepithelial current in an ensemble of cells
203 (Fig. 2C). We note that gating friction generally depends on the activation time of the
204 transduction channels, not just on the gating force (8). Detailed analysis of the force-
205 displacement cycles suggests that the channel-activation time had increased by about 50%, on
206 average, when the friction force ϕ_{MAX} reached a saturating value upon application of a negative
207 transepithelial current (SI Appendix Fig. S4). The observed variation of hair-bundle friction
208 (Fig. 3E-F) thus resulted from modulation of both the channel-activation time and the gating
209 force (Fig. 2C).

210 The polarity of the current ramp was then reversed. As the negative current increased, the
211 set-point deflection increased and the point of inversion symmetry in the force-displacement

212 cycle showed a nearly linear trajectory of slope 0.6 ± 0.2 pN $\cdot$ nm^{-1} ($n = 8$; Fig. 3C and D).
213 In addition, the signatures of gating compliance and gating friction, associated to nonlinear
214 force-displacement relations, were retrieved. The nonlinearity, however, reappeared at a
215 negative current with a smaller absolute value than that necessary to conceal the signatures of
216 channel-gating forces on the descending ramp. Over an ensemble of $n = 8$ cells, we measured
217 a shift in the transepithelial current of 2.3 ± 0.8 μA, corresponding to a 20-mV difference of
218 endolymphatic potential. Thus, the transition between states of strong and weak gating force
219 displayed hysteresis (Fig. 3E).

220 **Transition kinetics between the two states.**

221 To characterize the kinetics of the transition between states of strong and weak gating force, we
222 applied large negative steps of transepithelial current, here $I = -8$ μA (Fig. 4), while
223 continuously measuring a hair bundle's force-displacement cycle in response to triangular
224 mechanical stimulation. As expected from the effects of current ramps (Fig. 3), the force-
225 displacement cycle shifted in the negative direction along the displacement axis and the force-
226 displacement cycle lost the signatures of gating compliance and gating friction (Fig. 4A, SI
227 Appendix Movie S2). The time courses of the average hair-bundle position on the cycle, $\bar{X}$, and
228 of the maximal friction force, ϕ_{MAX}, were quantified by measuring the $10 - 90\%$ decay and
229 rise times following the onset and offset of the current step, respectively. Over an ensemble of
230 $n = 4$ hair cells, the characteristic time, $\tau_X^{ON} = 500 \pm 50$ ms, of negative hair-bundle motion
231 evoked by the current step was fivefold longer than that, $\tau_X^{OFF} = 100 \pm 30$ ms, necessary to
232 return to the initial position after the current was turned off (Fig. 4B). The friction force, ϕ_{MAX},
233 showed an opposite behavior: its decay time, $\tau_\Phi^{ON} = 180 \pm 40$ ms, after the onset of the current
234 step was twofold shorter than its rise time, $\tau_\Phi^{OFF} = 400 \pm 100$ ms, during recovery (Fig. 4B).
235 Note that the time required to measure a force-displacement cycle was here of only 20 ms. This
236 duration was about ten times shorter than $\tau_\Phi^{OFF/ON}$ and thus short enough to ensure a quasistatic
237 assessment of hair-bundle mechanics (Methods).

238 There was thus a separation of timescales between the changes of $\bar{X}$ and ϕ_{MAX}. At the onset
239 of the current step, gating compliance vanished before the negative shift had completed:
240 $\tau_\Phi^{ON}/\tau_X^{ON} = 0.37 \pm 0.17$ (Fig. 4B and C). In contrast, after the external transepithelial current
241 was turned off, the mechanical nonlinearity recovered more slowly than the average position of
242 the hair bundle: $\tau_\Phi^{OFF}/\tau_X^{OFF} = 4.2 \pm 2$ (Fig. 4B and C).

243 **Reducing the endolymphatic Ca^{2+} concentration replicates the effects of a negative**
244 **endolymphatic potential.**
245 A negative endolymphatic potential may have mediated its effects on the gating force by
246 reducing the magnitude of the Ca^{2+} influx through the transduction channels. To test this
247 hypothesis, we used iontophoresis of a Ca^{2+} chelator to reduce the endolymphatic Ca^{2+}
248 concentration near a hair bundle and thus the Ca^{2+} influx through the channels. In response to
249 descending and ascending ramps of iontophoretic current (Fig. 5A), or equivalently of Ca^{2+}
250 concentration, we again observed an increase in hair-bundle friction followed by a reversible
251 but hysteretic transition between states of strong and weak gating force (Fig. 5B and C, SI
252 Appendix Movie S3). Repeating the experiments over an ensemble of $n = 8$ cells confirmed
253 the robustness of these effects (Fig. 5D) and how they mirrored those observed upon
254 modulation of the endolymphatic potential (Fig. 3). In addition, the force-displacement relation
255 of a hair bundle could show strong gating compliance under control conditions but reversibly
256 become linear upon step application of a Ca^{2+} chelator, with no noticeable change in the linear
257 stiffness of the hair bundle (Fig. 5E). The same behavior was observed in $n = 7$ hair cells. Thus,
258 enough calcium in endolymph was required for the hair bundle to evince strong gating forces.

259 **DISCUSSION**

260 Our findings indicate that the endolymphatic potential can serve as a control parameter of the
261 gating force and thus of mechanosensitivity of the hair cell to deflections of its hair bundle.
262 This bioelectric effect is large: the gating force could nearly double upon application of negative
263 potentials and, conversely, be reduced by up to 80% of the control value at positive potentials
264 (Fig. 2F). Furthermore, we report here an unexpected and remarkable transition between a state
265 of strong gating forces, for which a hair bundle displayed a prominent nonlinear region of gating
266 compliance in its force-displacement relation and produced spontaneous oscillations, and a state
267 of weak gating force associated to linear mechanics and quiescence. This transition happened
268 over a timescale of a few hundred milliseconds (Fig. 4) when the endolymphatic potential
269 became more negative than a critical value, $U = U_C \simeq -50$ mV, corresponding to an applied
270 transepithelial current $I = I_C \simeq -5$ μA (Figs. 1D, 2C, 3C, and 3E). Reducing the Ca^{2+}
271 concentration near a hair bundle resulted in similar effects on gating compliance and gating
272 friction (Fig. 5), indicating that negative endolymphatic potentials modulated the gating force
273 by reducing the Ca^{2+} influx through the transduction channels.

Within the framework of the gating-spring model (SI Appendix Fig. S1A), the gating force for the whole hair bundle, $F_G = K_{GS}D$, is the product of the combined stiffness of the gating springs, K_{GS}, and of the gating swing, D, of a transduction channel. Note that these parameters are here expressed along the horizontal axis of mechanical stimulation. A major finding of our work is that the relative effect of an endolymphatic potential on the gating force was much larger than that on the hair-bundle stiffness (Fig. 2D): the gating force could vary by as much as about $\pm 100\%$, whereas stiffness in the same hair bundles varied only from -10% to $+25\%$. Because the gating springs are expected to contribute a significant fraction of the total hair-bundle stiffness (24), K, we reasoned that the change in gating force resulted mainly from a change in the magnitude of the gating swing. We could confirm this inference by measuring the hair-bundle stiffness, $K_{SP} = 0.17 \pm 0.03\ \mathrm{pN \cdot nm^{-1}}$ $(n = 14)$ $\simeq 0.2\ K$, after disruption of the tip links. By subtracting the average value of K_{SP} to individual measurements of K, we could then estimate, for each hair bundle, the gating-spring stiffness $K_{GS} = K - K_{SP}$, and in turn the gating swing D. After projection along the oblique axis of the tip links using the projection factor $\gamma = 0.14$ (25), we found a gating swing $d = \gamma D = 3.7 \pm 1.4\ \mathrm{nm}$ $(n = 29)$ under control conditions (SI Appendix Fig. S5A). Replicating the behavior of the gating force, the gating-swing change displayed a strong negative correlation with the endolymphatic potential (Pearson correlation $r = -0.86$; p-value $= 1 \cdot 10^{-10}$). The gating swing d could reach a value of up to about 8 nm in the presence of a negative endolymphatic potential or, conversely, be as small as 2 nm upon application of a potential of opposite polarity (SI Appendix Fig. S5B).

As recognized earlier (16), the gating swing can be nearly one order of magnitude larger than the expected diameter of the transduction channels' pore, which has been estimated at about 1.2 nm (2). Hair cells thus appear to have implemented a mechanism to magnify the conformational change associated to opening and closing of the transduction channel's pore, a feature also relevant to other mechanosensitive channels (26). In hair cells, the ion channels that mediate mechanoelectrical transduction are part of a molecular complex that includes TMC1—the pore-forming subunit (27), TMIE, CIB2, LHFPL5 and the lower end of the tip link, PCDH15 (28, 29). In addition, the complex may comprise two copies of each protein, forming a dimeric assembly with an axis of twofold symmetry (30, 31), thus corresponding to at least 10 proteins. Whether interactions between the multiple components of the transduction apparatus can lead to a collective rearrangement upon opening of the channel's pore, effectively

306 producing a large gating swing, remains unclear. Alternatively, channel gating has been
307 proposed to elicit a membrane-mediated interaction between two channel complexes, each
308 attached to one strand of the PCDH15 dimer, leading to large movement within the membrane
309 that magnifies the apparent gating swing (32).

310 Whatever the molecular substrate for the gating swing, our work indicates that the
311 transepithelial potential and the extracellular calcium concentration can modulate the
312 magnitude of the movement associated to channel gating (SI Appendix Fig. S5). In addition,
313 under conditions for which the calcium influx through the channels becomes too low, we found
314 that the gating swing drops to undetectable levels. This observation suggests that the channel-
315 protein complex must be primed by enough intracellular calcium to elicit a large swing, perhaps
316 via Ca^{2+} sensing by CIB2—the calcium- and integrin-binding protein (33). Hysteresis upon a
317 continuous back-and-forth variation of the endolymphatic potential (Fig. 3) or of the
318 extracellular concentration (Fig. 5) provides further support for the bistability of the channel-
319 protein complex.

320 Like other epithelia, the sensory epithelia that house the hair cells in the vertebrate inner ear
321 are polar tissues that experience a transepithelial potential under natural conditions. This
322 potential generally lies within a range $1 - 10$ mV, except in the mammalian cochlea where the
323 endolymphatic potential can reach $+100$ mV (34). In our experiments on frog saccular hair
324 cells, we applied endolymphatic potentials within a range of ± 100 mV. While this range
325 departs from natural conditions, varying the endolymphatic potential afforded a means to
326 reversibly and robustly control the electric field in the membrane near the transduction channels
327 and in turn the electromotive force that controls the magnitude of transduction currents,
328 including the Ca^{2+} influx into the hair cell.

329 Calcium is known to affect the operating point of the transducer and the kinetics of the active
330 adaptation process that drives active hair-bundle motility (4, 15, 18, 21–23, 35). Moreover,
331 there is also some evidence that the extracellular calcium concentration can modulate the
332 stiffness of the hair bundle (23, 24, 36). In our experiments, negative endolymphatic potentials
333 produced effects on spontaneous hair-bundle oscillations (SI Appendix Fig. S3) that were
334 qualitatively similar as those reported earlier in response to depolarization of the hair cell (37)
335 or to a decrease of the Ca^{2+} concentration in endolymph (18). Conversely, positive
336 endolymphatic potentials produced similar effects as hyperpolarization of the hair cell or
337 increasing the endolymphatic Ca^{2+} concentration. Previous models had postulated stiffer gating

338 springs at lower Ca^{2+} (18, 38), in apparent contradiction with recent in-vitro measurements of
339 PCDH15 elasticity (39). Our observations suggest instead that the effect of Ca^{2+} on gating-
340 spring stiffness was small compared to that on the gating swing, at least under our experimental
341 conditions.

342 In summary, our work demonstrates that the mechanical correlate of channel gating—the
343 gating force—can be modulated continuously and reversibly in the same hair cell upon variation
344 of the endolymphatic potential or calcium concentration. In addition, our observations reveal
345 that the transduction channels can operate in one of two functional states: a low-sensitivity state,
346 characterized by gating swings of about one nanometer or less and linear hair-bundle
347 mechanics, and a high-sensitivity state, where gating swings can be up to ten times larger,
348 corresponding to the emergence of active hair-bundle movements. Altogether, our findings
349 indicate that force sensitivity of the transduction channel protein complex—the fundamental
350 determinant of hair-cell mechanosensitivity—can be adjusted by the hair cell upon changes of
351 physiological control parameters.
352

METHODS

Experimental preparation.

Details of the experimental preparation have been published elsewhere (18, 23). Briefly, an excised preparation of the frog's saccule (Rivan 92 (40)) was glued with tissue-compatible surgical glue (Histoacryl, B. Braun) over a ~1 mm hole in a plastic disk (SI Appendix, Fig. S2A). The preparation was then secured in a two-compartment chamber, which exposed the apical and basal aspects of the sensory tissue to fluids with different ionic compositions to mimic physiological conditions. The basal bodies of the hair cells were bathed in artificial perilymph, a standard saline solution containing (in mM): 110 NaCl, 2 KCl, 1.5 $CaCl_2$, 3 D-glucose and 5 Hepes. Hair bundles instead projected into artificial endolymph with (in mM): 2 NaCl, 118 KCl, 0.25 $CaCl_2$, 3 D-glucose, and 5 Hepes. Each solution had a pH of ~ 7.3 and an osmotic strength of ~ 225 $\mathrm{mmol} \cdot \mathrm{kg}^{-1}$. To disconnect the hair bundles from the overlying otolithic membrane, the apical surface of the preparation was exposed for 20 min to endolymph supplemented with 67 $\mu\mathrm{g} \cdot \mathrm{mL}^{-1}$ of the protease subtilisin (type XXIV, Sigma). The otolithic membrane was then peeled off to obtain access to individual hair bundles. Experiments were performed at a temperature of 20°C.

Microscopic apparatus and mechanical stimulation.

The preparation was viewed through a $\times 60$ water-immersion objective of an upright microscope (BX51WI, Olympus). The mechanical properties of single hair bundles were characterized using published methods (8, 23). In short, the tip of a stimulus fiber was affixed to the kinociliary bulb of an individual hair bundle and imaged at a magnification of $\times$ 944 onto a displacement monitor comprising a dual photodiode. Stimulus fibers were fabricated from borosilicate capillaries (TW120-3, World Precision Instrument) and coated with a thin layer of gold-palladium to enhance contrast (Hummer 6.1, Anatech ltd.). The fiber was secured by its base to a stack-type piezoelectric actuator (PA-8/14, Piezosystem Jena) driven by a custom-made power supply (Elbatech). Its stiffness, k_F, was estimated from the analysis of thermal fluctuations at the fiber's tip.

In a first stimulation protocol, a series of step displacements, Δ, was applied to the fiber's base. The standard protocol consisted in the application of 7 to 9 successive pairs of step displacements in opposite directions with a magnitude growing with a constant increment, within the range $20 - 40$ nm. The force, $F = k_F\,(\Delta - X)$, and the bundle's displacement, X,

were estimated $5 - 9$ ms after the stimulus onset. This time was long enough for the open probability of the transduction channels to have reached a new steady state and for the frictional contribution to the applied force to have vanished, but short enough to limit the effect of adaptation. The resulting force-displacement relation, $F(X)$, was fitted by the equation (5, 15):

$$F = KX - F_G/[1 + \exp(-(X - X_0)/\delta)] + F_\emptyset, \quad (1)$$

from which we estimated the bundle's linear stiffness, K, the gating force, F_G, for the whole hair bundle, and the set-point deflection, X_0. The parameter $F_\emptyset$ ensured that $F = 0$ at $X = 0$. Because we did not use displacement-clamp feedback to stabilize positions of negative stiffness (16), the characteristic displacement, δ, could not be exploited. In this protocol, both photodiode and command signals were acquired and generated at a sampling rate of 2.5 kHz and the half-power frequency of the lowpass filter was fixed at 1 kHz. A force-displacement relationship was obtained by averaging 7 to 15 repetitions of the same stimulation protocol, which collectively took 10 to 20 seconds.

In a second stimulation protocol, we applied a symmetric triangular waveform of motion to the fiber's base, at a frequency of either 40 Hz or 100 Hz and with a peak-to-peak amplitude within the range $600 - 1000$ nm. The force applied to the hair bundle was estimated using a detailed description of the fiber's vibrational modes (8). This protocol resulted in force-displacement cycles with counterclockwise circulation. The half-height at any position, X, in the cycle provides an estimate of the average friction force $\phi(X) = [F^+(X) - F^-(X)]/2$ impeding the hair bundle motion at this position, where $F^\pm(X)$ represents the force in the positive and negative half cycle of stimulation, respectively. The friction force displayed a maximum, $\phi_{\mathrm{MAX}} = \phi(X_0)$, at a displacement that was identified earlier as the set-point deflection X_0 in Equation 1 (8). The force-displacement cycle also displayed a point of inversion symmetry of coordinates $(X_0,\ F_0 = [F^+(X_0) + F^-(X_0)]/2)$. The shift, ΔX, between the positions where the hair-bundle speed reached a maximal value, $|dX/dt| = V_{MAX}$, in the positive and negative half cycle of stimulation provided an estimate of the activation time of the transduction channels, $\tau = \Delta X/(2V_{MAX})$ (8). In this protocol, the force-displacement cycle was averaged over ten periods of the triangular stimulus at 40 Hz or, when a fast assessment of hair-bundle mechanics became necessary (as for the data shown in Fig. 4), over only two periods of a 100-Hz stimulus. Both photodiode and command signals were acquired and

generated at sampling rate of 25 kHz. The half-power frequency of the filter was fixed at 12.5 kHz for the photodiode signals and 0.5 kHz for the command signals.

Control of the transepithelial current and potential.

Using a current source (Linear Stimulator Isolator A395, World Precision Instruments) connected to a pair of silver chloride electrodes (SI Appendix Fig. S2A), we applied steps of transepithelial current with a magnitude that was varied within a range of ± 10 μA. In some preparations, we measured the transepithelial potential, $U(t)$, evoked by a step of transepithelial current, $I_{STEP} = 1$ μA (Fig. S2B), using an additional pair of electrodes connected to the headstage of a differential amplifier (voltage gain $\times$ 50; Model 3000, Systems Inc). The time course of the transepithelial potential was well described by an exponential relation $U(t) = U_{MAX} \exp(-t/\tau)$, with a characteristic timescale $\tau = 230 \pm 50$ μs (mean $\pm$ SD, n =13). Over an ensemble of 13 saccules, we found a transepithelial resistance $R = U_{MAX}/I_{STEP} = 10 \pm 2$ kΩ and capacitance $C = 23 \pm 4$ nF. Thus, over the range of transepithelial currents that we explored, the potential into the artificial endolymph that bathed the hair bundles—the endolymphatic potential— varied within a range of ± 100 mV with respect to the potential in the perilymphatic compartment.

In other experiments, we applied successive ramps of descending and ascending transepithelial currents at an absolute rate within the range of $0.5 - 0.9$ μA $\cdot$ s^{-1}. These rates were low enough to ensure that the variation of the transepithelial current remained small during the time required for probing hair-bundle mechanics, allowing these mechanical measurements to remain quasistatic. The minimal current was maintained for $1 - 2.5$ s before the ascending ramp started.

Iontophoresis of a calcium chelator.

We used iontophoresis of a calcium chelator to decrease the extracellular calcium concentration in the vicinity of individual hair bundles (9, 23). Coarse microelectrodes were fabricated from borosilicate capillaries (TW120F-3, World Precision Instrument) with a pipette puller (P97, Sutter Instrument); their resistance ranged from 0.8 to 1.5 MΩ when filled with 3-M KCl and immersed in the same solution. The electrode's tip was positioned at ~3 μm from the hair bundle.

In a first series of experiments, the electrodes were filled with 400-μM pentasodium triphosphate. Triphosphate allowed to decrease the calcium concentration while preserving the integrity of the tip links (23). A holding current of +10 nA was continuously applied to

445 counteract the diffusive release of the calcium chelator from the electrode, to which we added
446 either a step or a succession of descending and ascending ramps of iontophoretic current. The
447 steps had a magnitude of varying between -80 nA and-60 nA, while the ramps reached a
448 minimal value between -90 nA and-50 nA. The current varied at the same rate on the
449 descending and ascending ramps, within a range $5 - 8\ \mathrm{nA} \cdot \mathrm{s}^{-1}$, and the minimal current was
450 maintained for $1 - 2$ s before the ascending ramp started.

451 In a second series of experiments, we aimed at disrupting the tip links to evaluate their
452 contribution to hair-bundle stiffness. In this case, the electrode was filled with EDTA at a
453 concentration of 100 mM. We applied current steps of -100 nA on top of a resting current of
454 $+10$ nA. In three cells, reducing the amplitude of the step to about -35 nA allowed to maintain
455 the integrity of the tip links, adding data to those obtained with iontophoresis of triphosphate to
456 evaluate the effects of reducing the calcium concentration on a force-displacement relation.

457 **Signal generation and acquisition.**

458 All signals were generated and acquired under the control of a computer running a user interface
459 programmed with the LabVIEW software (version 2011, National Instruments). Command
460 signals were produced by a 16-bit interface card (PCI-6733, National Instruments). A second
461 16-bit interface card (PCI-6250, National Instruments) conducted signal acquisition. Sampling
462 rates for signal generation and acquisition varied within the range $2.5 - 25$ kHz. All signals
463 were conditioned with an eight-pole Bessel antialiasing filter (Model 3384, Krohn-Hite
464 Corporation) at a lowpass cut-off frequency set at half the sampling frequency unless otherwise
465 indicated.

466 **Analysis of spontaneous hair-bundle oscillations**

467 Details of the analysis of the spontaneous oscillations have been published elsewhere (20).
468 Briefly, the displacement, $X(t)$, of an oscillating hair bundle was monitored over a duration of
469 $10 - 30\ s$. The relation between its power spectrum, $C(f)$, and frequency, f, was first
470 smoothed by a moving average with a frequency window of 1 Hz and then fitted by the sum of
471 two Lorentzians

$$\tilde{C}(f) = \frac{A}{(f_0/2Q)^2 + (f - f_0)^2} + \frac{A}{(f_0/2Q)^2 + (f + f_0)^2}. \qquad (2)$$

472 The fit provided values for the quality factor Q, the characteristic frequency f_0, and parameter
473 A, which is related to the root-mean-square magnitude $X_{RMS} = \langle X(t) - \langle X(t)\rangle^2\rangle =$

$\int_{-\infty}^{+\infty} \tilde{C}(f)df = \sqrt{4\pi AQ/f_0}$ of the movement. In cases where it was bimodal, the probability density of hair bundle positions was fitted by the sum of two Gaussian functions. The fractional area under the Gaussian that was centered at a positive position with respect to the mean bundle position provided a functional estimate of the open probability P_O^{SS} of transduction channels at steady state.

ACKNOWLEDGEMENTS:

This research was supported by the Fondation pour l'Audition (project n°FPA RD 2020-7) and Labex Cell(n)Scale (ANR-11-LABX-0038 and ANR-10-IDEX-001-02). Achille Joliot is an alumni of the Paris Sciences et Lettres University and acknowledges a grant from the doctoral school "Ecole Doctorale Paris Ile de France" (EDPIF).

485 **REFERENCE**

486 1. A. J. Hudspeth, How the ear's works work. *Nature* **341**, 397–404 (1989).

487 2. R. Fettiplace, K. X. Kim, The physiology of mechanoelectrical transduction channels in
488 hearing. *Physiol. Rev.* **94**, 951–86 (2014).

489 3. P. Martin, G. A. Manley, "Auditory processing by the cochlea" in *Principles of Neural*
490 *Science*, McGraw-Hill Education / Medical; 6th edition, (2021), pp. 594–624.

491 4. D. P. Corey, A. J. Hudspeth, Kinetics of the receptor current in bullfrog saccular hair cells.
492 *J. Neurosci.* **3**, 962-976. (1983).

493 5. V. S. Markin, A. J. Hudspeth, Gating-spring models of mechanoelectrical transduction by
494 hair cells of the internal ear. *Annu. Rev. Biophys. Biomol. Struct.* **24**, 59–83 (1995).

495 6. J. Howard, A. J. Hudspeth, Compliance of the hair bundle associated with gating of
496 mechanoelectrical transduction channels in the bullfrog's saccular hair cell. *Neuron* **1**,
497 189-199. (1988).

498 7. A. J. Ricci, A. C. Crawford, R. Fettiplace, Mechanisms of active hair bundle motion in
499 auditory hair cells. *J. Neurosci.* **22**, 44–52 (2002).

500 8. V. Bormuth, J. Barral, J.-F. Joanny, F. Julicher, P. Martin, Transduction channels' gating
501 can control friction on vibrating hair-cell bundles in the ear. *Proc. Natl. Acad. Sci. USA*
502 **111**, 7185–7190 (2014).

503 9. M. Tobin, A. Chaiyasitdhi, V. Michel, N. Michalski, P. Martin, Stiffness and tension
504 gradients of the hair cell's tip-link complex in the mammalian cochlea. *eLife* **8**, e43473
505 (2019).

506 10. M. Beurg, E. T. Schwalbach, R. Fettiplace, LHFPL5 is a key element in force transmission
507 from the tip link to the hair cell mechanotransducer channel. *Proc. Natl. Acad. Sci. USA*
508 **121**, e2318270121 (2024).

509 11. I. J. Russell, M. Kossl, G. P. Richardson, Nonlinear mechanical responses of mouse
510 cochlear hair bundles. *Proc. R. Soc. Lond. B* **250**, 217–27. (1992).

511 12. D. K. Chan, A. J. Hudspeth, Ca2+ current–driven nonlinear amplification by the
512 mammalian cochlea in vitro. *Nat. Neurosci.* **8**, 149–155 (2005).

513 13. H. J. Kennedy, A. C. Crawford, R. Fettiplace, Force generation by mammalian hair
514 bundles supports a role in cochlear amplification. *Nature* **433**, 880–883 (2005).

515 14. P. Martin, A. J. Hudspeth, Active hair-bundle movements can amplify a hair cell's
516 response to oscillatory mechanical stimuli. *Proc. Natl. Acad. Sci. USA* **96**, 14306–14311
517 (1999).

15. P. Martin, A. J. Hudspeth, Mechanical frequency tuning by sensory hair cells, the receptors and amplifiers of the inner ear. *Annu. Rev. Condens. Matter Phys.* **12**, 29–49 (2021).

16. P. Martin, A. D. Mehta, A. J. Hudspeth, Negative hair-bundle stiffness betrays a mechanism for mechanical amplification by the hair cell. *Proc. Natl. Acad. Sci. USA* **97**, 12026–12031 (2000).

17. P. Martin, A. J. Hudspeth, F. Julicher, Comparison of a hair bundle's spontaneous oscillations with its response to mechanical stimulation reveals the underlying active process. *Proc. Natl. Acad. Sci. USA* **98**, 14380–14385 (2001).

18. P. Martin, D. Bozovic, Y. Choe, A. J. Hudspeth, Spontaneous oscillation by hair bundles of the bullfrog's sacculus. *J. Neurosci.* **23**, 4533–4548 (2003).

19. D. Ramunno-Johnson, C. E. Strimbu, L. Fredrickson, K. Arisaka, D. Bozovic, Distribution of frequencies of spontaneous oscillations in hair cells of the bullfrog sacculus. *Biophys. J.* **96**, 1159–68 (2009).

20. J. Barral, F. Jülicher, P. Martin, Friction from transduction channels' gating affects spontaneous hair-bundle oscillations. *Biophys. J.* **114**, 425–436 (2018).

21. N. Hacohen, J. A. Assad, W. J. Smith, D. P. Corey, Regulation of tension on hair-cell transduction channels: displacement and calcium dependence. *J. Neurosci.* **9**, 3988-3997. (1989).

22. A. J. Ricci, Y. C. Wu, R. Fettiplace, The endogenous calcium buffer and the time course of transducer adaptation in auditory hair cells. *J. Neurosci.* **18**, 8261–77 (1998).

23. J.-Y. Tinevez, F. Jülicher, P. Martin, Unifying the various incarnations of active hair-bundle motility by the vertebrate hair cell. *Biophys. J.* **93**, 4053–4067 (2007).

24. R. E. Marquis, A. J. Hudspeth, Effects of extracellular Ca2+ concentration on hair-bundle stiffness and gating-spring integrity in hair cells. *Proc. Natl. Acad. Sci. USA* **94**, 11923–11928 (1997).

25. R. A. Jacobs, A. J. Hudspeth, Ultrastructural correlates of mechanoelectrical transduction in hair cells of the bullfrog's internal ear. *Cold Spring Harb. Symp. Quant. Biol.* **55**, 547–561 (1990).

26. Y. R. Guo, R. MacKinnon, Structure-based membrane dome mechanism for Piezo mechanosensitivity. *eLife* **6**, e33660 (2017).

27. B. Pan, *et al.*, TMC1 forms the pore of mechanosensory transduction channels in vertebrate inner ear hair cells. *Neuron* **99**, 736-753.e6 (2018).

28. W. Zheng, J. R. Holt, The mechanosensory transduction machinery in inner ear hair cells. *Annu. Rev. Biophys.* **50**, 31–51 (2021).

553 29. X. Qiu, U. Müller, Sensing sound: Cellular specializations and molecular force sensors.
554 *Neuron* **110**, 3667–3687 (2022).

555 30. J. Ge, *et al.*, Structure of mouse protocadherin 15 of the stereocilia tip link in complex
556 with LHFPL5. *eLife* **7**, e38770 (2018).

557 31. H. Jeong, *et al.*, Structures of the TMC-1 complex illuminate mechanosensory
558 transduction. *Nature* **610**, 796–803 (2022).

559 32. F. Gianoli, T. Risler, A. S. Kozlov, Lipid bilayer mediates ion-channel cooperativity in a
560 model of hair-cell mechanotransduction. *Proc. Natl. Acad. Sci. USA* **114**, E11010–E11019
561 (2017).

562 33. R. Vallone, G. Dal Cortivo, M. D'Onofrio, D. Dell'Orco, Preferential binding of Mg2+
563 over Ca2+ to CIB2 triggers an allosteric switch impaired in Usher syndrome type 1J.
564 *Front. Mol. Neurosci.* **11**, 274 (2018).

565 34. C. Köppl, V. Wilms, I. J. Russell, H. G. Nothwang, Evolution of endolymph secretion and
566 endolymphatic potential generation in the vertebrate inner ear. *Brain. Behav. Evol.* **92**, 1–
567 31 (2018).

568 35. Y. C. Wu, A. J. Ricci, R. Fettiplace, Two components of transducer adaptation in auditory
569 hair cells. *J Neurophysiol* **82**, 2171–81 (1999).

570 36. M. Beurg, J.-H. Nam, A. Crawford, R. Fettiplace, The actions of calcium on hair bundle
571 mechanics in mammalian cochlear hair cells. *Biophys. J.* **94**, 2639–2653 (2008).

572 37. S. W. Meenderink, P. M. Quinones, D. Bozovic, Voltage-mediated control of spontaneous
573 bundle oscillations in saccular hair cells. *J. Neurosci.* **35**, 14457–66 (2015).

574 38. Y. Roongthumskul, L. Fredrickson-Hemsing, A. Kao, D. Bozovic, Multiple-timescale
575 dynamics underlying spontaneous oscillations of saccular hair bundles. *Biophys. J.* **101**,
576 603–610 (2011).

577 39. Villasante, C. M., Deng, X., Cohen, J. E., Hudspeth, A.J., Nanomechanics of wild-type
578 and mutant dimers of the inner-ear tip-link protein protocadherin 15. *Proc. Natl. Acad.*
579 *Sci. USA* **121**, e2404829121 (2024).

580 40. A. Neveu, Suitability of European green frogs for intensive culture: Comparison between
581 different phenotypes of the esculenta hybridogenetic complex. *Aquaculture* **295**, 30–37
582 (2009).

583

584 **MAIN-FIGURE LEGENDS**

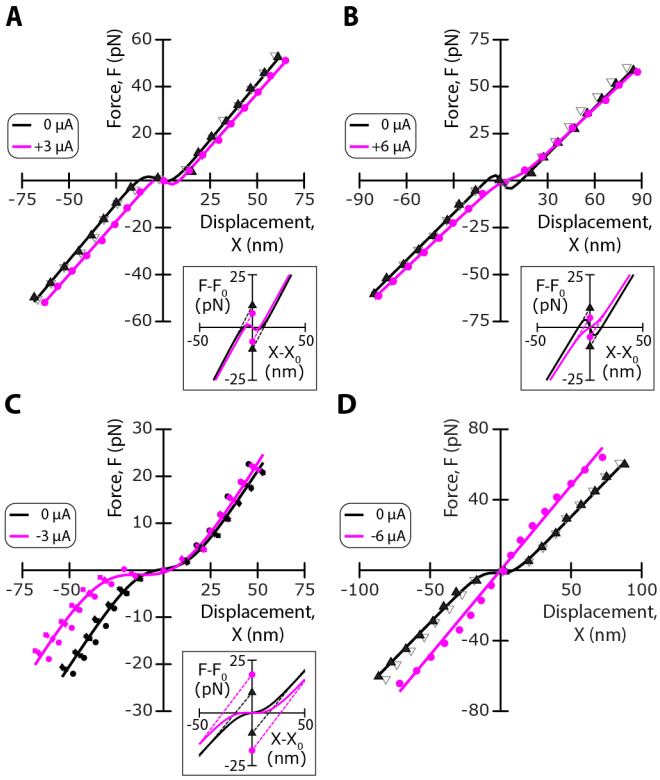

585

586 **Fig. 1 : Representative examples of mechanical changes evoked by a transepithelial**
587 **current.** (A-D) Force-displacement relations, $F(X)$, for four different hair bundles under
588 control conditions ($I = 0$ μA; black) and in the presence of a transepithelial current (magenta)
589 of amplitude $I = +3$ μA (A), $I = +6$ μA (B), $I = -3$ μA (C) and $I = -6$ μA (D). Each relation
590 was fitted by Equation 1 (solid lines; parameter values in SI Appendix Table S1). Insets: the
591 fitted curves are replotted with respect to the origin $(X_0, F(X_0))$, where X_0 is the set-point
592 deflection. Under each condition, the hair bundle's gating force, F_G, was given by the vertical
593 distance between the two symbols in the inset ($I = 0$: triangles; $I \neq 0$: disks). In (A), (B) and
594 (D), the open black symbols correspond to a measurement after restoring control conditions to
595 assess reversibility; in (C), the experiment was repeated 4 times.

596

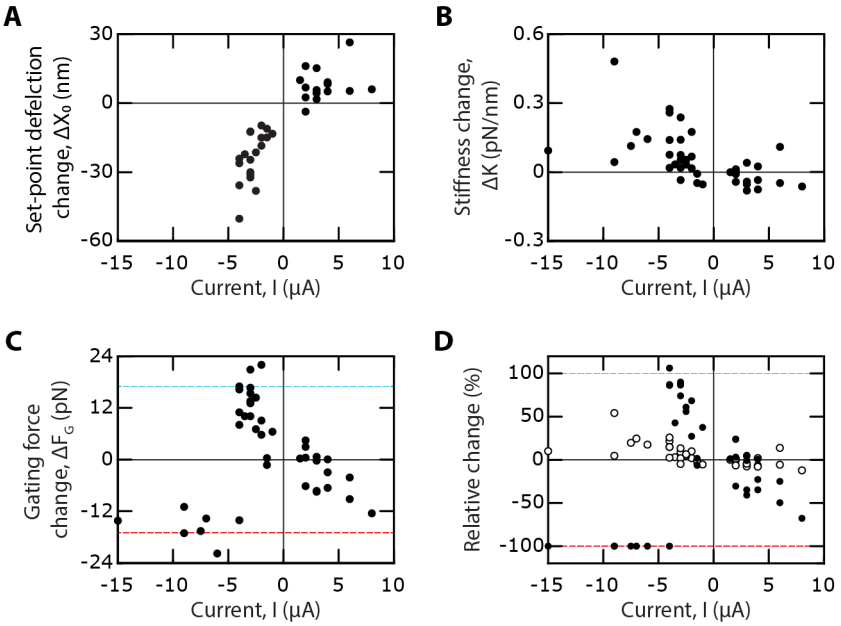

Fig. 2 : Changes in set-point deflection, stiffness and gating force upon application of a transepithelial current. (A) The change, ΔX_0, of the set-point deflection showed a strong positive correlation to the transepithelial current, I (Pearson correlation r $= 0.87$; p-value: $4 \cdot 10^{-11}$; $n = 34$). (B) The change, ΔK, of the linear stiffness was negatively correlated to the current, but only weakly (Pearson correlation r $= -0.57$; p-value: 10^{-4}; $n = 41$). (C) For I > -4 μA, the change, ΔF_G, of the bundle's gating force showed a strong negative correlation to the current (Pearson correlation r $= -0.86$; p-value: $8 \cdot 10^{-11}$; $n = 34$). (D) Relative change of the hair-bundle's gating force, $\Delta F_G / F_G(0)$ (solid disks) and linear stiffness, $\Delta K / K(0)$ (open disks) as a function of the transepithelial current, I. Under control conditions ($I = 0$), the gating force was $F_G = 17 \pm 4$ pN (mean $\pm$ SD, $n = 29$). In (C) and (D), the red and blue dashed lines mark, respectively, a reduction and an increase of the gating force by 100% with respect to the mean value under control conditions. For $I < -5$ μA, all the force displacement relations were linear: the gating force had dropped to undetectable levels and the set-point deflection could no longer be measured from the mechanics.

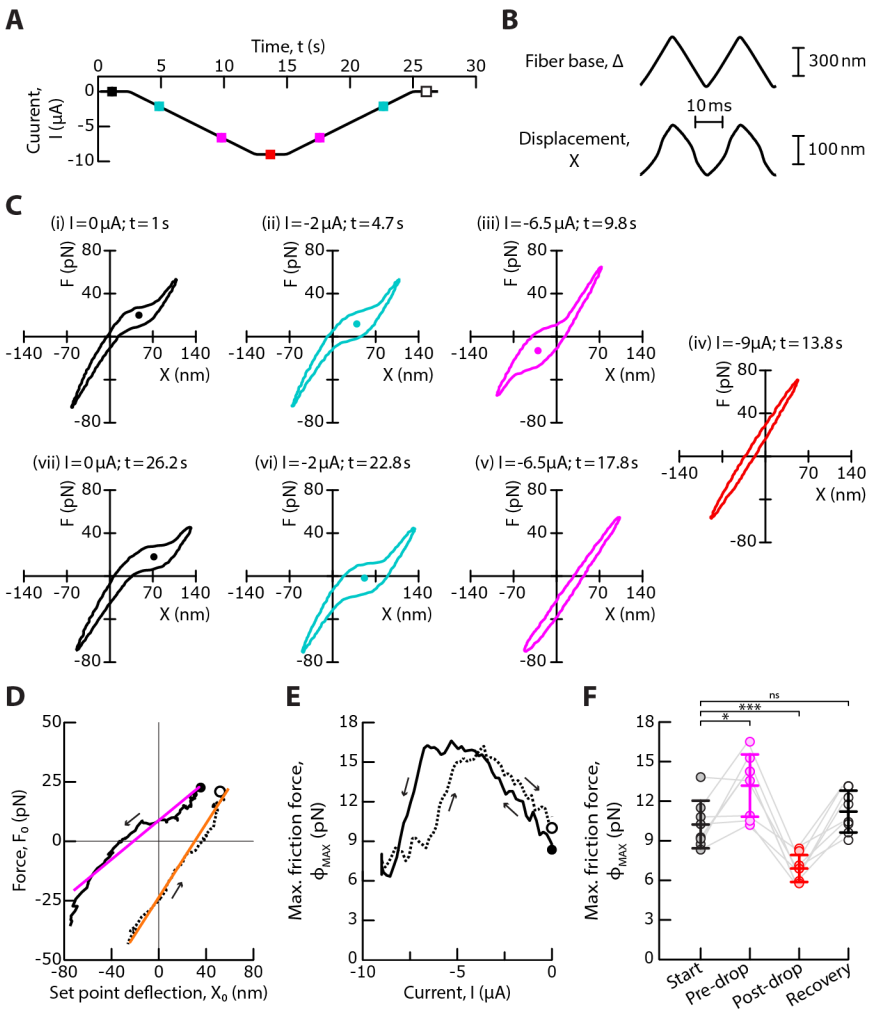

Fig. 3 : **Transition between states of strong and weak gating force.** (A) A descending ramp of a negative transepithelial current was followed by an ascending ramp of current at the same absolute rate of 0.9 $\mu A \cdot s^{-1}$. The colored square symbols indicate the time points of the analysis shown in (C). (B) The hair bundle was continuously moved back and forth (bottom) by imposing a periodic triangular movement to the stimulus fiber's base, here with a peak-to-peak amplitude of 600 nm and at a frequency of 40 Hz (top). The movements were averaged over 10 stimulus cycles. (C) Force-displacement cycles for the values of the transepithelial current and at times indicated at the top of each sub-panel (see colored square symbols in (A)). (D) Trajectory of the point of inversion symmetry (X_0, F_0) in a force-displacement cycle, marked by disks in (C). Linear fits to these trajectories: $F_0 = 0.41 \cdot X_0 + 9$ ($R^2 = 0.92$) (magenta) and $F_0 = 0.78 \cdot X_0 + 24$ ($R^2 = 0.98$) (orange), respectively. (E) Maximal friction force, ϕ_{MAX}, as a function of the transepithelial current, I. (F) For all the 8 different hair bundles that followed the same protocol, the maximal friction force, ϕ_{MAX}, first increased as the

transepithelial current decreased, before dropping to a low value as the hair bundle transitioned from a state of strong gating force to a state of weak gating force at more negative values of the current than a threshold $I = I_{DROP} = -3.7 \pm 1$ μA (mean $\pm$ SD, $n = 8$). Colored disks mark, for each hair-bundle, the value of ϕ_{MAX} at the start of the experiment ($I = 0$, black), before ($I = I_{DROP} + 1$ μA, magenta) and after ($I = -9$ μA, red) the drop of ϕ_{MAX}, and at the end of the experiment ($I = 0$ μA, white). Error bars: mean $\pm$ SD. Statistical significance was assessed using a paired t-test with p-values from left to right: $2 \cdot 10^{-2}$, $8 \cdot 10^{-4}$, 10^{-1}. ns > 0.05, * p-value ≤ 0.05, *** p-value ≤ 0.001. In (D-E), black solid and dashed lines correspond to the descending and ascending ramps of transepithelial currents, respectively. Arrows indicate the direction of circulation along the curve from start (black disk) to finish (white disk).

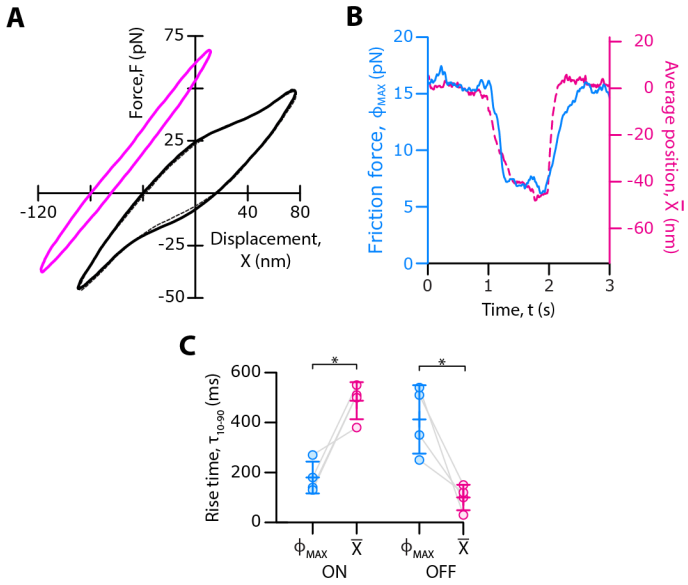

638

639 **Fig. 4 : Transition kinetics between states of strong and weak gating force.** (A) Force-
640 displacement cycle here averaged over 50 cycles of stimulation, under control conditions ($I =$
641 0; black solid line), 400 ms after the onset of a step of transepithelial current ($I = -8$ µA;
642 magenta) and 600 ms after termination of the current step ($I = 0$; black dashed line). (B) Time
643 course of the maximal friction force, ϕ_{MAX}, (blue line) and of the average displacement, $\bar{X}$,
644 (dashed magenta line) in a force-displacement cycle. The current step started at $t = 1$ s and
645 ended at $t = 2$ s. (C) Time, τ_{10-90}, required for the maximal friction force, ϕ_{MAX} (blue disks),
646 and the average displacement, $\bar{X}$ (magenta disks), to transition from 10% to 90% of the total
647 change after the onset (ON) and the termination (OFF) of a step of transepithelial current ($I =$
648 -8 µA). Error bars indicate the mean $\pm$ SD. Statistical significance was assessed using a
649 paired t-test with p-values from left to right: $2 \cdot 10^{-2}$, $3 \cdot 10^{-2}$; * p-value ≤ 0.05. The base of
650 the stimulus fiber followed a periodic triangular waveform of motion, with a peak-to-peak
651 amplitude of 600 nm and at a frequency of 100 Hz. For the data shown in (B) and (C), the
652 force-displacement cycles were averaged over only two cycles of stimulation.
653

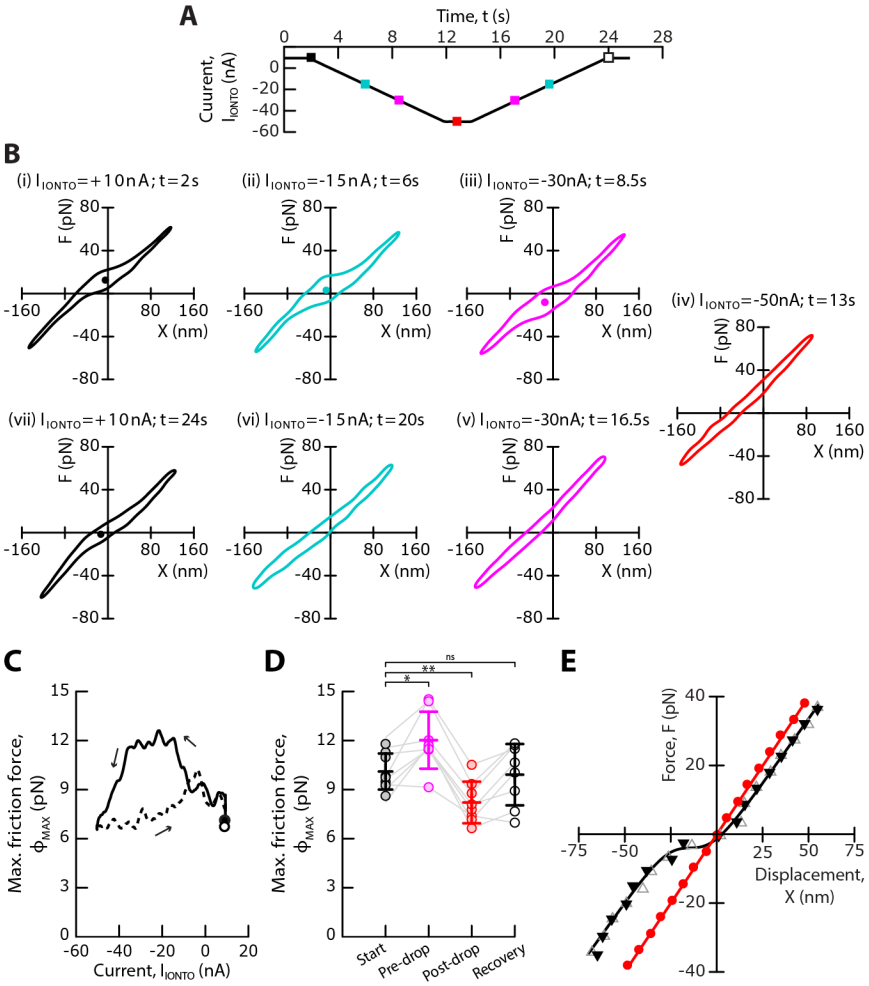

654

655 **Fig. 5 : Replicating the effects of negative endolymphatic potentials with iontophoresis of**
656 **a Ca^{2+} chelator.** (A) We used iontophoresis of a calcium chelator to decrease the extracellular
657 Ca^{2+} concentration in the vicinity of a hair bundle. A descending ramp of a negative
658 iontophoretic current, I_{IONTO}, which was carried in part by a Ca^{2+}chelator, was followed by an
659 ascending ramp of current at the same absolute rate of $6.6\ \mathrm{nA} \cdot \mathrm{s}^{-1}$. The colored square symbols
660 indicate the time points of the analysis shown in (B). (B) Each sub-panel shows the bundle's
661 force-displacement cycle in response to a triangular mechanical stimulus for the value of the
662 iontophoretic current, I_{IONTO}, and at the time, t, indicated at the top. (C) Maximal friction
663 force, ϕ_{MAX}, as a function of the iontophoretic current, I_{IONTO}, which varied in time from start
664 (black disk) to finish (white disk). Arrows indicate the direction of circulation along the curve.
665 Solid and dashed lines correspond to the descending and ascending ramps of iontophoretic
666 currents, respectively. (D) For all the 8 different hair bundles that followed the same protocol,
667 the maximal friction force, ϕ_{MAX}, first increased as the extracellular Ca^{2+} concentration

decreased, before dropping to a low value as the hair bundle transitioned from a state of strong gating force to a state of weak gating force at more negative values of the iontophoretic current than a threshold $I_{IONTO} = I_{DROP} = -40 \pm 10$ nA (mean $\pm$ SD, $n = 8$). Colored disks mark, for each hair-bundle, the value of ϕ_{MAX} at the start of the experiment ($I_{IONTO} = +10$ nA, black), before ($I_{IONTO} = I_{DROP} + 5$ nA, magenta) and after ($I_{IONTO} = -50$ nA, red) the drop of ϕ_{MAX}, and at the end of the experiment ($I_{IONTO} = +10$ nA, white). Error bars: mean $\pm$ SD. Statistical significance was assessed using a paired t-test with p-values from left to right: $1.5 \cdot 10^{-2}$, $5 \cdot 10^{-3}$, $6 \cdot 10^{-1}$; ns > 0.05; * p-value ≤ 0.05, ** p-value ≤ 0.01. (E) The force-displacement relation of a different hair bundle displays a region of gating compliance under control conditions (black triangles) but was linear in the presence of a steady iontophoretic current of -60 nA (red circle). This effect was reversible (grey triangles). Each force-displacement relation was fitted by Equation 1 (solid lines; parameter values in SI Appendix Table S1). In (B-D), a periodic triangular waveform of motion was applied to the base of the stimulus fiber, with a peak-to-peak amplitude of 600 nm and at a frequency of 40 Hz. In (E), force-displacement relations were instead measured in response to step displacements at the base of the stimulus fiber (see Methods).

Supporting Information for

Electrical control of the transduction channels' gating force in sensory hair cells.

Achille Joliot[a,b] , Laure Stickel[a,b] and Pascal Martin[a,b,*]

[a] Physique des Cellules et Cancer, Institut Curie, PSL Research University, CNRS UMR168, F-75248 Paris, France.

[b] Sorbonne Université, F-75252 Paris, France.

[*] Correspondence: pascal.martin@curie.fr

This PDF file includes:

Table S1

Figures S1 to S5

Legends for Movies S1 to S3

Other supporting materials for this manuscript include the following:

Movies S1 to S3

Supplementary Table

Table S1 Parameter values for fits of force-displacement relations with Equation 1.

Variable	Definition	Fig. 1A		Fig. 1B		Fig. 1C		Fig. 1D		Fig. 5E	
I (μA)	Transepithelial current	0	+3	0	+6	0	−3	0	−6	n/a	n/a
I_{IONTO} (nA)	Iontophoretic current,	n/a	n/a	n/a	n/a	n/a	n/a	n/a	n/a	+10	−60
X_0 (nm)	Set-point deflection	−3	1	1	+6	−0.2	−12.7	−2	n/a	−14	n/a
K ($\mathrm{pN \cdot nm^{-1}}$)	Stiffness	0.96	0.91	0.83	0.78	0.6	0.66	0.82	0.96	0.75	0.80
F_G (pN)	Gating force	21	13	18	9	19	36	22	n/a	22	n/a
δ (nm)	Characteristic length	4	2	2	5	8.9	13	6	n/a	7	n/a
$F_\emptyset$ (pN)	Force constant	14	5	7	0.6	10	25	11	n/a	18	n/a
R^2	Coefficient of determination	0.999	0.994	0.986	0.986	0.986	0.986	0.986	0.986	0.979	0.993

Supplementary Figures

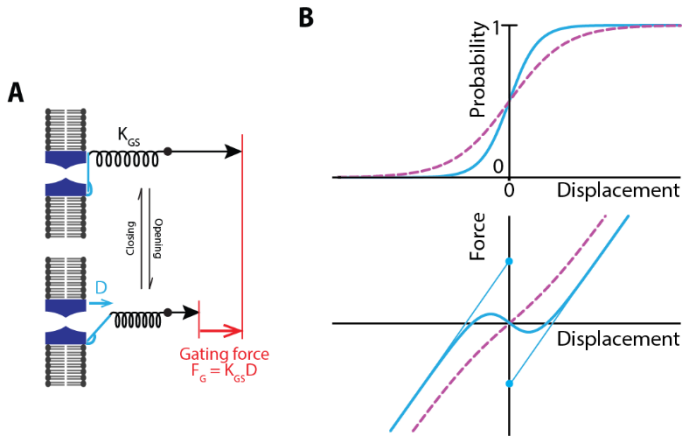

Fig. S1 : Gating-spring model of mechanoelectrical transduction. (A) The concept of gating force. When the transduction channels switch between their open and closed state, tension in the gating springs is reduced (black arrows); this mechanical correlate of channel gating is called the gating force, $F_G = K_{GS} \cdot D$ (red arrow), where K_{GS} is the combined stiffness of all the gating springs operating in parallel in the hair bundle and D is the gating swing of each channel. (B) Electrical and mechanical responses to hair-bundle displacement. Top: sigmoidal relationship of channel open probability to displacement in the case of weak (dashed magenta line) and strong (solid blue line) gating force. The larger the gating force, the steeper the sigmoid and the more sensitive the hair cell is to displacement of its hair bundle. Bottom: The force–displacement relationship displays a shallow nonlinearity when sensitivity is low (dashed magenta curve) and a strong nonlinearity when sensitivity is high (smooth blue curve). The gating force is given by the vertical shift between the two linear limbs of the force-displacement relation; it is here shown in the case of high sensitivity as the distance between the two disks.

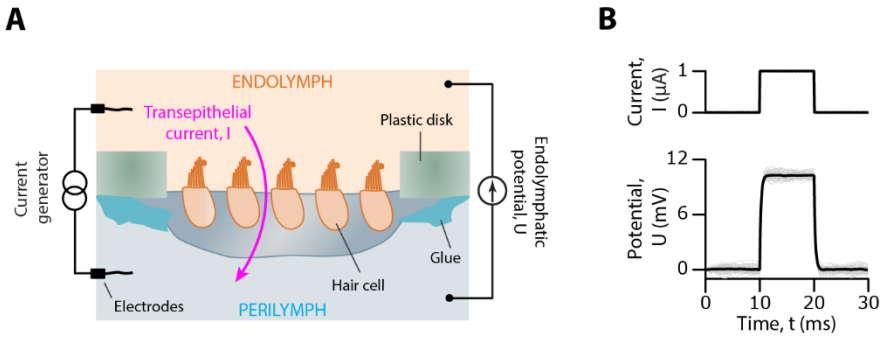

Fig. S2 : Two-compartment ex-vivo preparation of the frog saccule. (A) Schematic of the setup. The tissue was glued over a 1-mm hole in a plastic disk. Its apical and basal aspects were bathed in artificial endolymph and perilymph, respectively. A transepithelial current, I, was produced by a pair of silver chloride electrodes connected to a current generator, resulting in an endolymphatic potential, U, with respect to the potential in perilymph. The sign convention is such that positive currents lead to a positive value of the endolymphatic potential. (B) A +1-μA step of transepithelial current (top) evoked an endolymphatic potential $U \simeq +10$ mV at steady state (bottom, grey), corresponding to a transepithelial resistance of 10 kΩ. An exponential fit (black line), $U(t) = A\exp(-t/\tau)$, to the response yielded the amplitude $A =$ 10.2 mV and the characteristic time $\tau = 210$ μs.

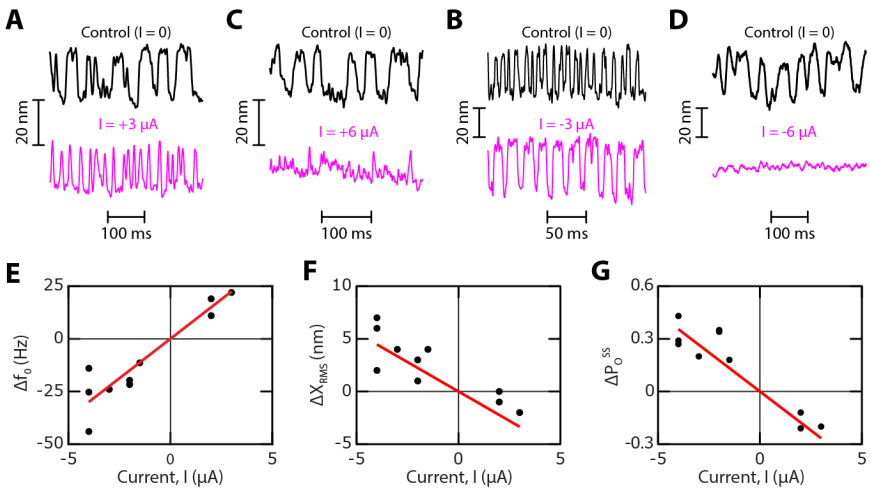

Fig. S3 : Effects of a transepithelial current on spontaneous hair-bundle oscillations. Under control conditions ($I = 0$), over an ensemble of $n = 10$ oscillatory hair bundles, the oscillations had a characteristic frequency $f_0 = 22 \pm 14$ Hz, a root-mean-squared (RMS) amplitude $X_{RMS} = 13 \pm 4$ nm and their bimodal position histograms were associated with a steady-state open probability for the transduction channels $P_O^{SS} = 0.4 \pm 0.1$, thus close to $1/2$. These characteristics are remarkably similar to those reported earlier with hair cells from a different frog species (18, 20). (A-D) Representative examples of spontaneous hair-bundle oscillations under control conditions ($I = 0$; top) and in the presence of a transepithelial current (bottom) $I = +3$ μA (A), $I = +6$ μA (B), $I = -3$ μA (C), and $I = -6$ μA (D). (E) The change, Δf_0, of the oscillation frequency displayed a strong positive correlation to the transepithelial current (Pearson correlation $r = +0.9$; p-value $= 10^{-4}$; $n = 10$). (F) The change, ΔX_{RMS}, of the RMS amplitude of spontaneous oscillations displayed a strong negative correlation to the transepithelial current (Pearson correlation $r = -0.9$; p-value $= 1 \cdot 10^{-3}$; $n = 10$). (G) The change, ΔP_O^{SS}, of the open probability at steady state displayed a strong negative correlation to the transepithelial current (Pearson correlation $\mathrm{r} = -0.9$, p-value $= 1 \cdot 10^{-4}$, $n = 10$). In (A), the transepithelial current evoked an increase of the oscillation frequency from 17 Hz to 39 Hz, a decrease of the RMS amplitude of oscillation from 7 nm to 5 nm and a decrease of the steady-state open probability from 0.5 to 0.3. Conversely in (B), the frequency of oscillation decreased from 49 Hz to 25 Hz, the RMS amplitude of oscillation increased from 11 nm to 15 nm and the steady-state open probability increased from 0.4 to 0.6. In the presence of a large positive current ($I = +6$ μA; panel B), the hair bundle only produced irregular spiky movements in the positive direction: the transduction channels were closed most of the time and evinced brief openings. Instead, a large negative current ($I = -6$ μA; panel D) completely abolished

spontaneous oscillations. Red lines in (E-G) correspond to proportional fits of respective slopes $7\ \mathrm{Hz} \cdot \mu\mathrm{A}^{-1}$ ($R^2 = 0.86$; panel E), $-1.1\ \mathrm{nm} \cdot \mu\mathrm{A}^{-1}$ ($R^2 = 0.6$; panel F), and $-0.08\ \mu\mathrm{A}^{-1}$ ($R^2 = 0.83$; panel G).

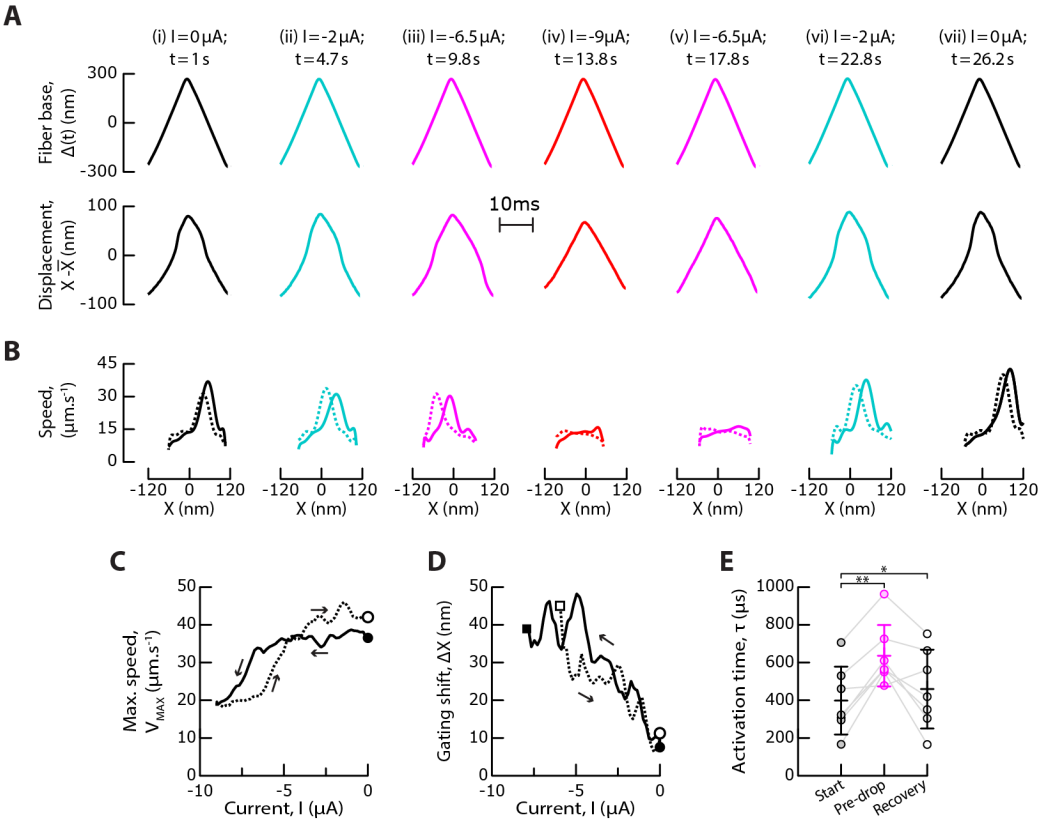

Fig. S4 : Effect of a transepithelial current on the channel-activation time. Same data as in Fig. 3A-E, to which this figure is associated. The time course of successive ramps of descending and ascending transepithelial current can be found in Fig. 3A. (A) Fiber-base displacement, Δ (*top*), and hair-bundle displacement, X (*bottom*), as a function of time for one stimulus cycle at time points and values of the transepithelial current indicated at the top of each time trace. (B) Hair-bundle speed, $|dX/dt|$, on the positive (*solid line*) and negative (*dashed line*) half cycles of mechanical stimulation as a function of displacement, X. The distance between the two peaks, ΔX, defines the gating shift. (C-D) Maximum speed, V_{MAX} (C), and gating shift, ΔX (D), as a function of the transepithelial current, I, which varied in time from start (black disk) to finish (white disk). Arrows indicate the direction of circulation along the curve. Solid and dashed lines correspond to the descending and ascending ramps of transepithelial currents, respectively. In panel (D), a black square indicates the current at which the signatures of gating compliance and gating friction vanished on the descending ramp; bellow this current, the gating shift is no longer defined. Conversely, a white square indicates recovery of the signatures of gating compliance and gating friction on the ascending ramp. (E) For the same ensemble of hair bundles as in Fig. 3, the distributions of the estimated activation time of the transduction channel, $\tau = \Delta X/(2\, V_{MAX})$, are shown at the start of the experiment ($I = 0$, black), before the

drop of the maximal friction force (magenta, see Fig. 3F), and at the end of the experiment ($I = 0$, white). Error bars: mean $\pm$ SD. Statistical significance was assessed using a paired t-test with, from p-values from left to right: $0.0014, 0.021$ *p-value ≤ 0.05, **p-value ≤ 0.01.

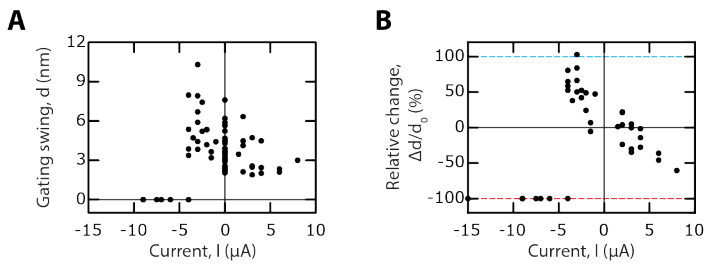

Fig. S5: Electrical control of the gating swing. The gating swing, d, (A) and its relative change, $\Delta d/d_0$, (B) are shown as a function of the transepithelial current, I, where $\Delta d = d(I) - d(I = 0)$ and $d_0 = d(I = 0)$. For $I \geq -5$ μA, the relative change displayed a strong negative correlation to the current (Pearson correlation $r = -0.86$; p-value: $1 \cdot 10^{-10}$). Same dataset as that used in Fig. 2. After each measurement of a bundle's force-displacement relation, the gating swing was estimated as $d = \gamma F_G/(K - K_{SP})$, where F_G and K are respectively the gating force and linear stiffness resulting from a fit of the force-displacement relation with Equation 1 and K_{SP} is the mean stiffness measured over an ensemble of hair bundles after disruption of their tip links. The projection factor $\gamma = 0.14$ was used to estimate the gating swing along the oblique axis of the tip link.

802

803 **Legends for supplementary movies**

804

805 **Movie S1 (separate file): Transition between states of strong and weak gating force.** Movie
806 associated to Fig. 3A-E. The force-displacement cycle in response to triangular mechanical
807 stimulation of the hair bundle (top) is shown over time as the transepithelial current follows
808 successive descending and ascending ramps (bottom). The friction force, $\phi(X)$, at each
809 displacement X of the hair bundle is color coded as indicated on the right; it is given by the
810 half-height of the force-displacement cycle. To obtain smooth videos, the force-displacement
811 cycles were here averaged over 15 cycles, instead of 10 cycles in the data shown in Fig. 3.

812 **Movie S2 (separate file): Kinetics of the transition between states of strong and weak**
813 **gating force.** Movie associated to Fig. 4A-B. The force-displacement cycle in response to
814 triangular mechanical stimulation of the hair bundle (top) is shown over time before, during
815 and after application of a negative step of transepithelial current (bottom). The friction force,
816 $\phi(X)$, at each displacement X of the hair bundle is color coded as indicated on the right; it is
817 given by the half-height of the force-displacement cycle. The force-displacement cycles were
818 here averaged over 5 cycles.

819 **Movie S3 Transition between states of strong and weak gating force upon a decrease of**
820 **extracellular calcium concentration.** Movie associated to Fig. 5A-D. The force-displacement
821 cycle in response to triangular mechanical stimulation of the hair bundle (top) is shown over
822 time as an iontophoretic current trough a pipette containing a calcium chelator and positioned
823 near a hair bundle follows successive descending and ascending ramps (bottom). The friction
824 force, $\phi(X)$, at each displacement X of the hair bundle is color coded as indicated on the right;
825 it is given by the half-height of the force-displacement cycle. To obtain smooth videos, the
826 force-displacement cycles were here averaged over 15 cycles, instead of 10 cycles for the data
827 shown in Fig. 5.

828